Magnetic Resonance in Medicine 67:1316–1323 (2012)

Reduced Field of View MRI with Rapid, B_1-Robust Outer Volume Suppression

Travis B. Smith* and Krishna S. Nayak

MRI scans are inefficient when the size of the anatomy under investigation is small relative to the subject's full extent. The field of view must be expanded, and acquisition times accordingly prolonged. Shorter scans are feasible with reduced field of view imaging (rFOV) using outer volume suppression (OVS), a magnetization preparation sequence that attenuates signal outside a region of interest (ROI). This work presents a new OVS sequence with a cylindrical ROI, short duration, and improved tolerance for B_1^+ inhomogeneity. The sequence consists of a nonselective adiabatic tipdown pulse, which provides B_1^+-robust signal suppression, and a fast 2D spiral cylindrical tipback pulse. Analysis of the Bloch equations with transverse initial magnetization reveals a conjugate symmetric constraint for tipback pulses with small flip angles. This property is exploited to achieve two-shot performance from the single-shot tipback pulse. The OVS sequence is validated in phantoms and in vivo with multislice spiral imaging at 3 T. The relative signal-to-noise ratio efficiency of the proposed sequence was 98% in a phantom and 75–90% in vivo. The effectiveness is demonstrated with cardiovascular rFOV imaging, which exhibits improved resolution and reduced artifacts compared to conventional, full field of view imaging. Magn Reson Med 67:1316–1323, 2012. **© 2011 Wiley Periodicals, Inc.**

Key words: outer volume suppression; reduced field of view imaging; spiral imaging; RF pulse design

Spatial aliasing will occur in an MR image if the *k*-space sample spacing is not fine enough to support the full spatial extent of the received signal. This sampling criterion becomes burdensome and inefficient when the region of interest (ROI) is small relative to the full spatial extent of the anatomy. With reduced or restricted field of view (rFOV) imaging, efficiency can be improved. In an rFOV acquisition, the prescribed FOV is decreased to more closely match the ROI size, thereby permitting shorter readout durations (T_{read}), fewer *k*-space segments, or both. The time savings can be leveraged for faster acquisitions, improved tolerance to artifacts from motion or off resonance, finer spatial resolution, and/or better coverage.

Many rFOV techniques employ outer volume suppression (OVS), a spatial presaturation sequence which attenuates signal outside the ROI and serves as a spatial anti-aliasing filter (1). Energy along the readout direction is suppressed by hardware filters, so typically OVS is applied to reduce signal along the direction(s) orthogonal to the readout. Compared to multidimensional excitation pulses, whose long durations can negate the time-efficiency benefit of an rFOV acquisition (2,3), OVS preparations are applied before a set of readout intervals (TR) and generally provide more design flexibility.

Our goal was to develop an OVS design suitable for multislice cardiovascular spiral imaging at 3 T. Cardiovascular imaging is archetypal of the need for rFOV acquisitions. For example, fine resolution is required for coronary artery imaging, yet resolution is limited because most of the acquisition time must be spent avoiding aliasing from the surrounding anatomy. At 3 T and higher field strengths, where increased SNR can be traded for finer resolution, effective OVS is challenging due to the greater inhomogeneities in the RF transmit (B_1^+) field and main magnetic (B_0) field. Furthermore, with cardiac imaging and other time-sensitive protocols, there is a strong incentive to keep the duration of the OVS sequence to a minimum.

Many existing OVS sequences are effective only at lower field strengths ($\leq$1.5 T) due to their sensitivity to B_1^+ inhomogeneity, or have long durations that preclude their utilization in cardiac and other rapid imaging applications. Dynamic radial acquisitions with REST (4), which uses cosine-modulated saturation pulses to reduce the FOV orthogonal to each spoke, has been applied in 1.5 T cardiac imaging (5); however, this method is not suitable for spiral imaging, must be applied once each TR interval, and in general is B_1^+ sensitive. A faster, single-sided OVS design, which has been used in rapid single-shot spin-echo cardiac imaging, is also not robust to B_1^+ variation (6). The BISTRO method (7) is capable of 2D OVS with improved B_1^+ field insensitivity, but its duration is over 200 msec. A 1D OVS design has been used for spinal cord diffusion imaging at 3 T (8), however the duration is almost 100 msec due to the need for multiple quadratic-phase pulses (9).

Pisani et al. used a rapid OVS sequence for functional MRI of the fetal brain at 1.5 T (10). The OVS design consists of a long 2D spatially selective spiral tipdown pulse (11) followed by a B_1^+-insensitive adiabatic half-passage tipback pulse (12,13) and spoiler gradients. The sequence suppresses signal outside of a cylindrical ROI, and is ideally suited for multislice spiral or radial imaging.

In this work, we propose a new 2D OVS preparation sequence that addresses the challenges of rFOV imaging at 3 T. The sequence uses an adiabatic pulse and a spiral pulse to achieve OVS with a cylindrical ROI, similar to (10). However, in the proposed design, the tipdown pulse is adiabatic and the tipback pulse is spatially

Ming Hsieh Department of Electrical Engineering, University of Southern California, Los Angeles, California, USA.

*Correspondence to: Travis B. Smith 3740 McClintock Ave, EEB 412, University of Southern California, Los Angeles, CA 90089-2564.
E-mail: traviss@usc.edu

Received 22 April 2011; revised 15 June 2011; accepted 5 July 2011.

DOI 10.1002/mrm.23116

Published online 14 November 2011 in Wiley Online Library (wileyonlinelibrary.com).

© 2011 Wiley Periodicals, Inc.

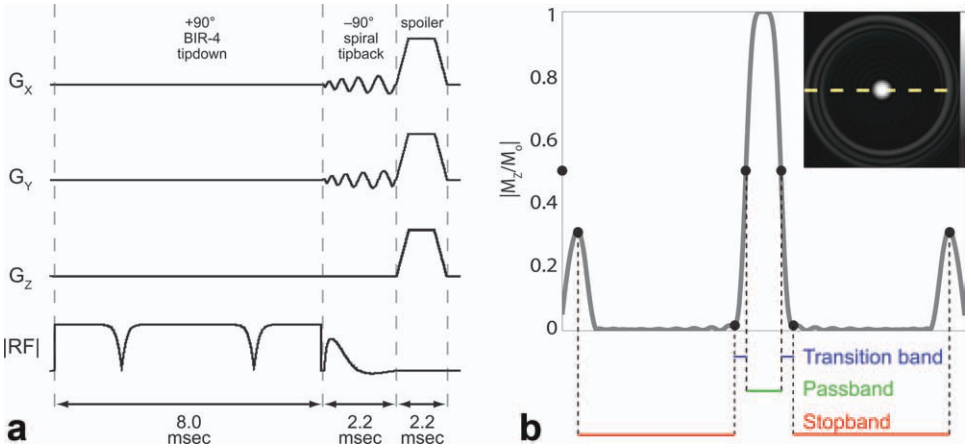

FIG. 1. **a**: Diagram of the OVS pulse sequence, which consists of a nonselective adiabatic tipdown pulse followed by a spatially selective tipback pulse. **b:** Spatial profile of the longitudinal magnetization (along the dashed line in the inset 2D profile) after OVS preparation.

selective. For small flip angles, tipback pulses can be significantly shorter than the more conventional tipdown pulses, as discussed below. The total duration of the RF pulses is 10.2 msec, which is 19% shorter than the 1.5 T OVS design proposed in (10). Also, the proposed design is more robust to B_1^+ inhomogeneity and has a larger saturation bandwidth for improved suppression performance at 3 T. We use a B_1-insensitive rotation type 4 (BIR-4) tipdown pulse (14). For a fixed RF power, a BIR-4 pulse has a larger bandwidth than a half-passage pulse (13), which increases suppression bandwidth and decreases the sensitivity to B_0 field variation.

We next discuss the proposed OVS sequence and details related to its implementation. We then evaluate its performance in phantoms and establish its utility within an rFOV imaging protocol. Finally, we evaluate in vivo performance and provide cardiovascular rFOV imaging examples at 3 T.

MATERIALS AND METHODS

OVS Design and Performance Measures

The proposed OVS pulse sequence consists of a nonselective adiabatic tipdown ($+90^\circ_x$) pulse followed by a 2D spatially selective tipback (-90°_x) pulse and dephasing gradients, as shown in Fig. 1a. The tipdown pulse rotates the longitudinal magnetizations of all spins in the scanning volume into the transverse plane. The tipback pulse then rotates spins within a cylindrical beam ROI back to a longitudinal orientation. Finally, spoiler gradients dephase the remaining transverse signal outside the ROI. The total duration of the OVS sequence is 12.4 msec. The spatial profile of the longitudinal magnetization after OVS preparation is depicted in Fig. 1b. Figure 2 shows the simulated performance of the OVS sequence across varying B_1^+ scale factors and resonance frequency offsets.

The OVS passband, stopband, and transition regions are defined in Fig. 1b. One measure of OVS performance is the stopband attenuation, defined as the ratio of stopband signal energy after OVS preparation to the energy with no preparation. Stopband attenuation, which affects the signal-to-noise ratio (SNR) within the ROI when the FOV is reduced, is primarily determined by the adiabatic tipdown pulse.

For spiral rFOV imaging, another OVS performance measure is the relative efficiency, defined as

$$\text{relative efficiency} = \frac{\mu_{\text{OVS}}}{\mu_{\text{baseline}}}, \qquad [1]$$

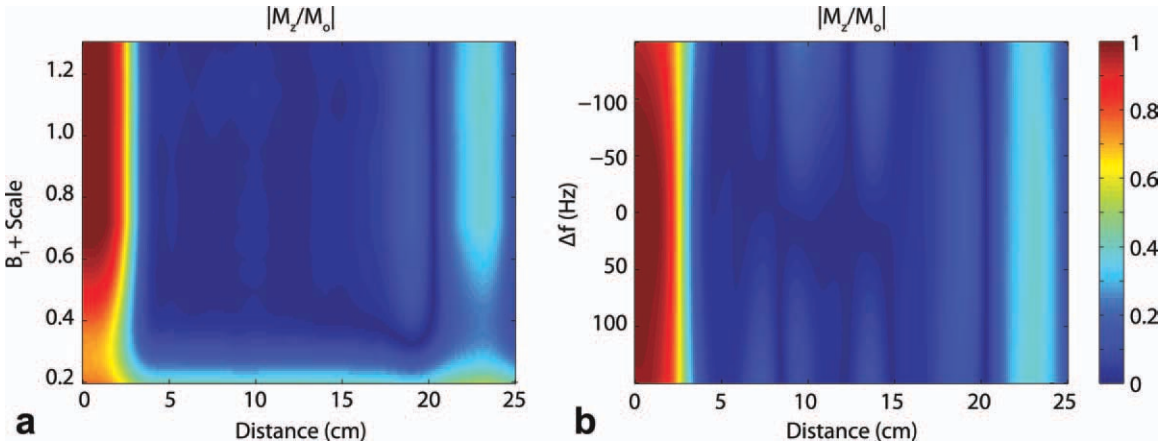

FIG. 2. The simulated longitudinal magnetization after OVS preparation demonstrates the robustness of the sequence. Distance $|r|$ is from the center of the OVS region of interest. The passband is $|r| < 2.5$ cm, and the stopband is 4 cm $< |r| <$ 20 cm. **a:** On resonance ($\Delta f = 0$ Hz) performance with varying B_1^+ scale. **b:** Off resonance performance with B_1^+ scale = 1.0.

where $\mu = \mathrm{SNR}/(\rho^2\sqrt{T_{acq}})$ is the SNR efficiency. The relative efficiency is the additional passband SNR loss after accounting for changes in acquisition time (T_{acq}) and image resolution (ρ), as compared to a full FOV baseline image without OVS preparation. We assume that for both the baseline and OVS acquisitions, TR $\gg T_1$ and the echo times (TE) are identical. When all imaging parameters are identical between the baseline and OVS scans, the relative efficiency becomes a measure of passband attenuation.

Tipdown Pulse Design

For B_1^+ robust suppression, we use an 8.0 msec +90° BIR-4 tipdown pulse (14) with hyperbolic tangent and tangent functions for the amplitude and frequency modulations ($\beta = 10$, $\tan(\lambda) = 130$) and a peak RF amplitude of 0.16 G. To preserve passband signal, the tipback pulse must be coherent with the passband transverse magnetization. Variation in the local B_1^+ and B_0 fields creates dispersion of the transverse magnetization phase, lowering the relative efficiency through unwanted stopband signal and incomplete tipback of the passband signal. The BIR-4 design parameters were chosen to maximize coherence and minimize the phase dispersion, defined as the difference between the maximum and minimum transverse phase, while maintaining an average suppression of 0.99 M_o across simulated B_1^+ scales from 0.5 to 1.0 and resonance offsets from −100 Hz to 100 Hz. These ranges represent the expected operational environment within the OVS passband for rFOV cardiovascular imaging (15). The OVS tipdown pulse has a phase dispersion of 42.9° over this range, and a bandwidth of 680 Hz.

Tipback Pulse Design

We use a 2.2 msec −90° 2D spiral pulse (11) for tipback with a cylindrical spatial profile, with time-bandwidth product of 4.0 and gradients spiraling outward to avoid passband attenuation due to T_2^+ decay. No rephasing lobe is necessary because all residual transverse magnetization will be gradient spoiled. The passband width is 5 cm, which is small enough to offer significant rFOV imaging benefits but still large enough both to image most vessels even with substantial variation in breath-hold positioning and to tolerate modest gradient delays. The two-sided stopband width is 40 cm, which is large enough to accommodate most body sizes and scan plane orientations. Gradients can be scaled to adjust the passband width (and transition and stopband widths) as necessary, provided hardware limits are not exceeded.

Unlike a conventional spiral excitation pulse, the single-shot tipback pulse has the effective performance of a two-shot pulse. The second spiral interleaf is generated by the rotation from the 2D transverse plane to the 1D longitudinal axis. The real-valued spatial profile of the longitudinal magnetization after a tipback pulse corresponds to a symmetry constraint in k-space. This phenomenon can be described in terms of the coupling between the spatial profiles of a conventional excitation (tipdown) pulse and a tipback pulse, which holds for all small-tip pulses (Appendix). The spatial profile of a tipdown pulse, $M_{xy}^d(\boldsymbol{r})$, with initial longitudinal magnetization M_o is related to the corresponding tipback pulse spatial profile, $M_z^b(\boldsymbol{r})$, through

$$M_z^b(\mathbf{r}) = -\cos\theta_o Re\left\{M_{xy}^d(\mathbf{r})\right\} + \sin\theta_o \mathrm{Im}\left\{M_{xy}^d(\mathbf{r})\right\}, \quad [2]$$

where $M_o e^{j\theta_o}$ is the initial transverse magnetization before the tipback pulse (Appendix). The tipback spatial profile is a combination of the tipdown real and imaginary components, which exhibit conjugate symmetry and antisymmetry, respectively, in excitation k-space (1). The symmetry constrains the k-space energy distribution and, for spiral pulses, establishes a second interleaf as shown in Fig. 3. The imaginary component contains the mainlobe and even sidelobes while the real component contains only the odd sidelobes. Because we want the tipback pulse to be in phase with component containing the mainlobe, we will refer to the imaginary component as the in-phase (or I) signal and the real component as the quadrature (or Q) signal. By proper tuning of the tipback RF phase, we can select the I signal—which effectively has twice the stopband width.

We leverage this additional performance for shorter pulse duration. A shorter pulse reduces T_2^+ decay in the passband and limits T_1 recovery in the stopband. To shorten the pulse, the gap between two spiral arms is increased until the desired stopband width is reached while satisfying hardware and safety constraints on the maximum gradient slew rate and peak RF amplitude. The 2.2 msec tipback pulse in the proposed OVS sequence has 1.95 times shorter duration than a conventional tipdown pulse with an equivalent spatial profile.

Imaging Experiments

All experiments were performed on a Signa Excite HD 3 T system (GE Healthcare, Waukesha, WI) with maximum gradient amplitude 40 mT/m and slew rate 150 T/m/sec. All acquisitions used body coil transmission and an 8-channel phased array cardiac coil for reception. Parallel imaging was not used.

To calibrate the OVS sequence, we acquired B_0 and B_1^+ maps in a breath-hold using the simultaneous multislice mapping approach in (16). Average values were calculated within a circular ROI representing the passband at the center of each map. The scanner center frequency was adjusted to compensate for frequency offsets. The transverse magnetization phase was estimated from the average B_1^+ scale using a lookup table of BIR-4 Bloch simulation results. The tipback RF phase was set to this value to isolate the I signal, and the tipback amplitude was adjusted to mitigate B_1^+ scaling.

Once the OVS sequence was calibrated, full FOV and rFOV imaging were performed using 2D multislice spoiled gradient echo acquisitions with uniform-density 16-shot spiral trajectories and spectral spatial RF excitation (17). All acquisitions had a 50° flip angle and 2.0 msec TE. Artificial gating was used for phantom acquisitions, and ECG gating was used for in vivo scans. One spiral shot was acquired each heartbeat (R-R interval) per slice, and the TR for each slice varied between 750 and 1000 msec depending on the R-R interval time. The

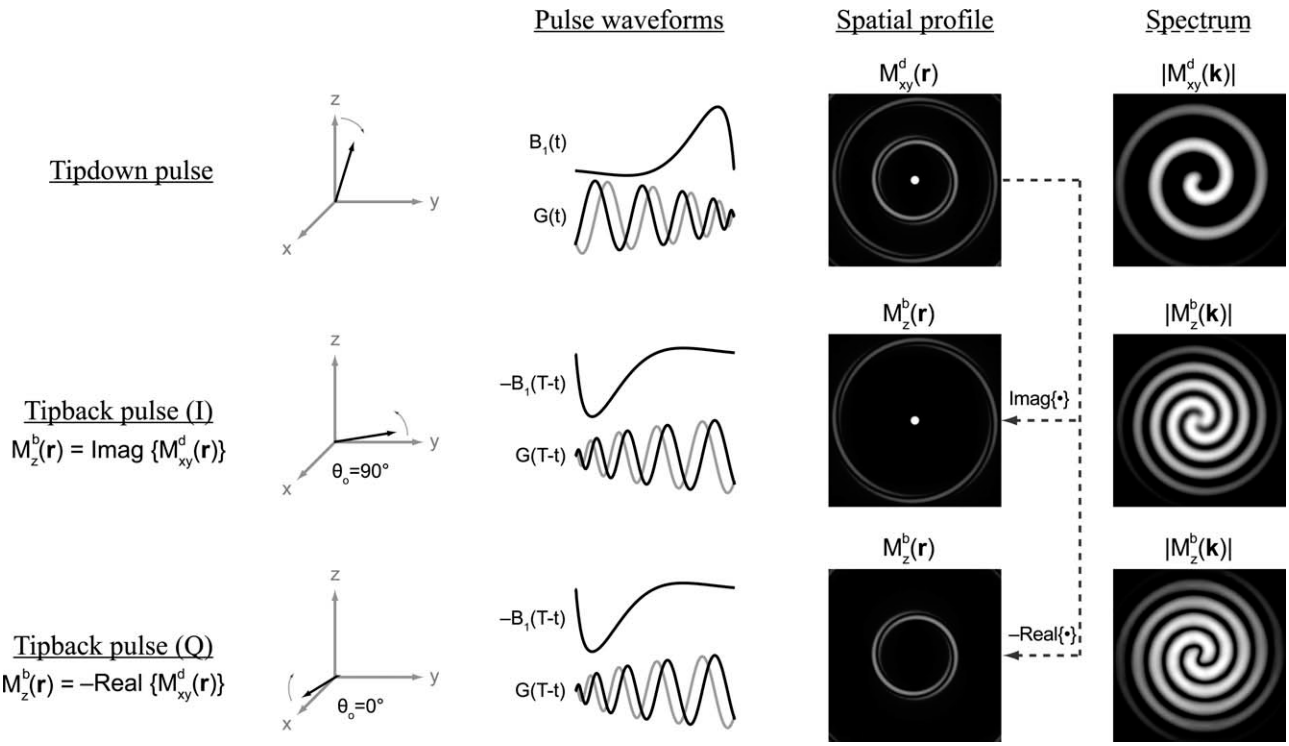

FIG. 3. Relationship between the tipdown spatial profile, $M^d_{xy}(\mathbf{r})$, and the tipback spatial profile, $M^b_z(\mathbf{r})$, for a simulated spiral pulse applied along $\hat{x}$. For any small-tip pulse, the tipback profile is equivalent to a weighted combination of the real and imaginary components of the tipdown profile. The weights depend on the tipback RF phase and on θ_o, the phase of the initial transverse magnetization. Due to conjugate-symmetry, the spectrum of the spiral tipback pulse contains a second interleaf, which doubles the distance between sidelobes in the spatial profile. This additional performance is leveraged to shorten the tipback pulse and reduce the duration of the OVS sequence.

OVS preparation was applied once each R-R interval immediately before the first slice-selective excitation pulse. Images were reconstructed on the scanner with compiled Matlab (Mathworks, Natick, MA) software using gridding with Jacobian density compensation (18). Image analysis and calculations of efficiency and stopband attenuation were done offline using Matlab.

OVS validation experiments were performed using a 27 cm diameter doped-water ball phantom (T_1 = 190 msec, T_2 = 30 msec) and a standard resolution phantom (T_1 = 250 msec, T_2 = 20 msec). In vivo performance was assessed with rFOV cross-sectional imaging of the descending aorta (DAo) and a linear segment of the right coronary artery (RCA) in two healthy volunteers. Both subjects were screened for MRI risk factors and provided informed consent in accordance with institutional policy. Three adjacent slices were acquired in each acquisition. Imaging parameters are shown in Table 1. For the DAo scans, the OVS passband was scaled to 9 cm to capture the vena cava. For coronary artery imaging, the

Table 1
Imaging Parameters for SNR Comparisons Among Experiments

Subject	Acquisition type	FOV (cm)	ρ (mm)	T_{read} (msec)	T_{acq} (msec)	Slice thickness (mm)	Figure
Res phantom	Full FOV	20	0.6	25.8	361.2	10.0	4c,d
Res phantom	Full FOV[a]	20	0.6	25.8	361.2	10.0	4e,f
Res phantom	rFOV[a]	20	0.6	5.3	74.2	10.0	4h
Ball phantom	Full FOV	36	3.0	4.1	49.2	10.0	4g
Ball phantom	Full FOV[a]	36	3.0	4.1	49.2	10.0	4i,j
DAo	Full FOV	32	2.0	6.1	85.4	10.0	5a,b
DAo	Full FOV[a]	32	2.0	6.1	85.4	10.0	5c,d
DAo	rFOV[a]	16	2.0	2.5	35	10.0	5e
DAo	rFOV[a]	16	1.15	5.7	79.8	10.0	5f
RCA	Full FOV	26	0.8	28.4	454.4	7.5	6a,b
RCA	Full FOV[a]	26	0.8	28.4	454.4	7.5	6c,d
RCA	rFOV[a]	13	0.8	7.1	113.6	7.5	6e
RCA	rFOV[a]	13	0.4	25.2	403.2	15	6f

All experiments used 16 spiral shots, 50° flip angle and TE = 2.0 mec, and TR = 750–1000 msec.
[a]OVS preparation was used.

Table 2
OVS Performance

Subject	Acquisition type	Expected relative SNR	Expected relative SNR (incl. T_2)	Stop-band atten.	SNR	Relative efficiency	Relative efficiency (incl. T_2)
Ball phantom	Full FOV	–	–	–	65.6	–	–
Ball phantom	Full FOV[a]	1.0	0.83	95%	53.1	81%	98%
DAo	Full FOV	–	–	–	45.2	–	–
DAo	Full FOV[a]	1.0	0.98	90%	39.7	88%	90%
DAo	rFOV[a]	0.64	0.63	–	21.3	74%	75%
DAo	rFOV[a]	0.32	0.31	–	11.6	80%	83%
RCA	Full FOV	–	–	–	22.8	–	–
RCA	Full FOV[a]	1.0	0.87	85%	16.2	71%	82%
RCA	rFOV[a]	0.50	0.43	–	7.7	68%	79%
RCA	rFOV[a]	0.47	0.41	–	7.1	66%	76%

The expected SNR factor is relative to the full FOV baseline scans without OVS.
[a]Indicates OVS preparation was used.

diastolic quiescent period was located with cine imaging before data collection, and respiratory motion was controlled with end-exhalation breath holds. The cross-sectional coronary artery images were reconstructed with frequency-segmented off resonance compensation (19) using 3.0 mm resolution field maps also acquired during the scan. Data were gridded with measured k-space trajectories (20) to reduce artifacts due to inaccurate generation of the gradient fields.

RESULTS

The OVS performance measures for each phantom and in vivo experiment are listed in Table 2. Intrinsic T_2 attenuation during the OVS sequence was assessed using the specified values for the phantoms and nominal T_2 values of 275 msec for blood in the DAo (21) and 40 msec for tissues surrounding the RCA (22). From Bloch simulation, we have measured the effective transverse duration time for the tipdown and tipback pulses to be 5.2 msec and 350 μsec, respectively. Thus the intrinsic passband signal loss including the 120 μsec interpulse hardware delay is $\exp(-5.67/T_2^+)$ for T_2^+ in milliseconds.

For the ball phantom, the measured B_1^+ scale in the 5 cm passband was 0.90 ± 0.11. The OVS stopband attenuation was 95%, and the relative efficiency was 81%. When intrinsic T_2 decay was considered, the efficiency was 98%. Images from both phantoms are shown in Fig. 4. Figure 4a,b show the I and Q signals acquired with the OVS passband width scaled to 1.9 cm to demonstrate the conjugate symmetry constraint described in Fig. 3. For the resolution phantom, the rFOV image of the comb object (Fig. 4h) has less blurring as compared to the full FOV image (Fig. 4d), even though both have the same prescribed resolution.

For the DAo experiments, the measured B_1^+ scale in the 9 cm passband was 0.82 ± 0.24 across the three slices. The OVS stopband attenuation was 90% and the relative efficiency was 88%, but 90% when T_2 decay was

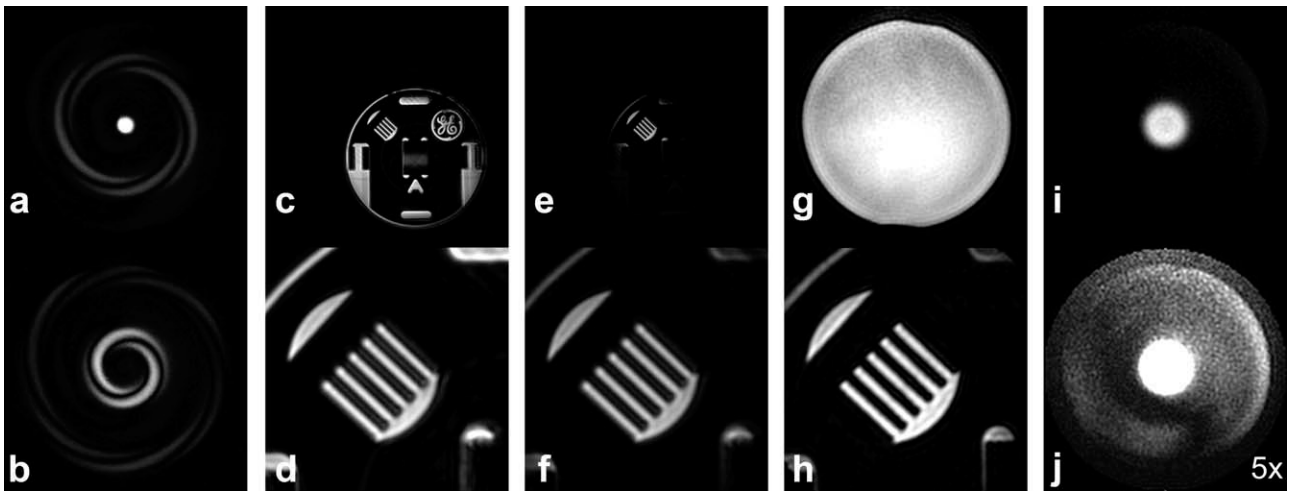

FIG. 4. OVS performance in phantoms. Ball phantom images with the OVS tipback gradients scaled to show the structure of the *I* (**a**) and *Q* (**b**) signals, acquired by selectively tuning the tipback pulse RF phase. Resolution phantom images with a full FOV before (**c**, detail of the comb in **d**) and after (**e**, detail in **f**) OVS preparation, and with a rFOV (**h**) at the same prescribed resolution. Off resonance blurring artifacts are not evident in the rFOV image. Ball phantom images with a full FOV before (**g**) and after (**i,j**) OVS preparation. Image (**j**) is 5× clipped to show the noise floor.

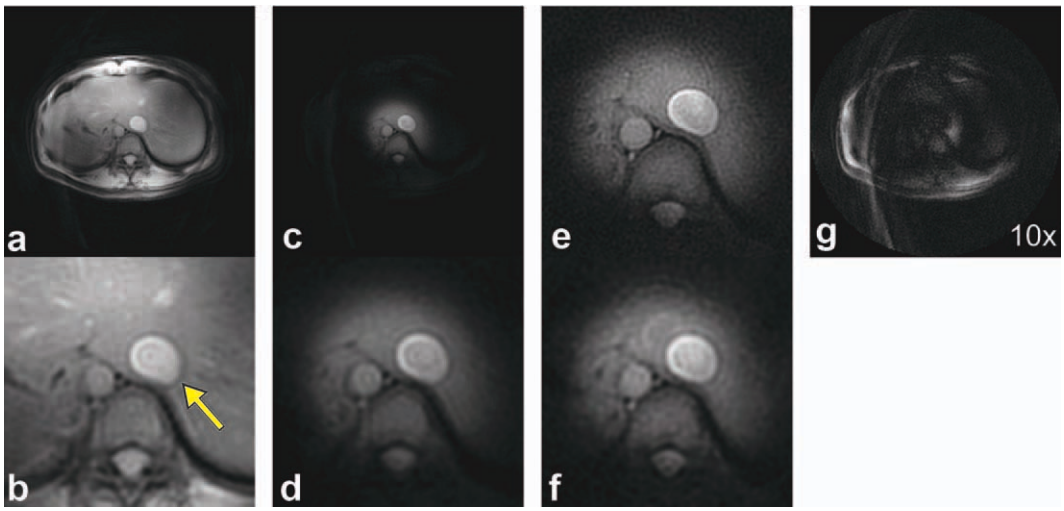

FIG. 5. OVS performance around the descending aorta. Images with a full FOV before (**a**, detail in **b**) and after (**c**, detail in **d**) OVS preparation, and with a rFOV (**f**) at the same prescribed resolution. A fine-resolution rFOV image (**e**) is also shown. Blurring and ringing artifacts around the vena cava (arrow) are less evident in both rFOV images. The *Q* signal (**g**), shown with 10× clipping, indicates that OVS calibration was successful and minimal passband signal was lost. [Color figure can be viewed in the online issue, which is available at wileyonlinelibrary.com.]

considered. Images from a representative slice are shown in Fig. 5. The rFOV images exhibit fewer artifacts, as seen around the vena cava, compared to the full FOV images. The accuracy of the OVS calibration is confirmed by the *Q* signal image (Fig. 5g), which shows little remaining passband energy compared to the *I* signal image (Fig. 5c).

For the RCA experiments, the measured B_1^+ scale in the 5 cm passband was 0.72 ± 0.25 across the three slices. The OVS stopband attenuation was 85% and the relative efficiency was 71%, but 82% when T_2 decay was considered. Images from a representative slice are shown in Fig. 6. The full FOV image (Fig. 6b) contains residual blurring artifacts which are not apparent in the rFOV image (Fig. 6f).

DISCUSSION

OVS performance degrades when B_1^+ scales are small (<0.3), the off resonance bandwidth is large (>300 Hz), or the tissue T_2^+ in the passband is short (<50 msec). Smaller B_1^+ scales limit the effectiveness of the tipdown and tipback pulses and cause greater dispersion of the passband transverse magnetization phase. Similarly, severe off resonance decreases the coherency between the transverse magnetization and the tipback pulse, causing the tipback of more Q signal and less I signal and, consequently, lower efficiency.

For these reasons, at field strengths higher than 3 T, the tipdown pulse should be re-optimized to balance phase coherence with pulse duration and intrinsic T_2^+ attenuation. Depending on the off resonance bandwidth,

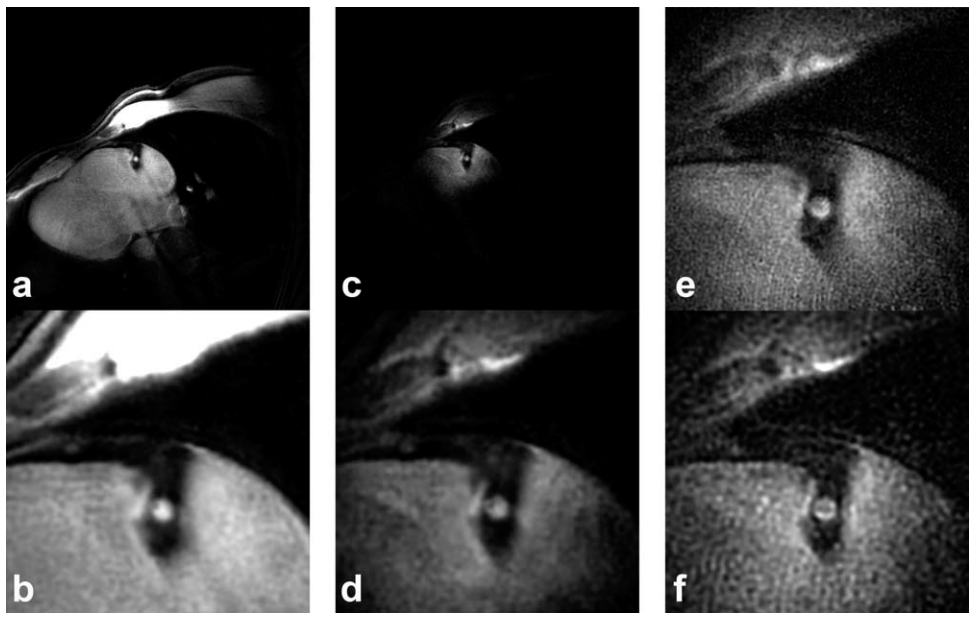

FIG. 6. OVS performance with coronary artery imaging and off resonance correction. Images will a full FOV image before (**a**, detail in **b**) and after (**c**, detail in **d**) OVS preparation, and with a rFOV prescribed with the same (**f**) and finer (**e**) resolution.

the delay between the tipdown and tipback pulses could be adjusted to improve the coherency. We investigated optimizing this delay, but found through Bloch simulation and experimental testing that the performance benefits at 3 T were negligible. At higher magnet strengths with greater field inhomogeneities, this may have a more significant impact.

The proposed OVS design is flexible and permits customization to many applications. A spiral tipback pulse makes the OVS ideally suited for polar trajectories, however a 1D tipback pulse could be used instead for B_1^+-robust OVS in Cartesian acquisitions. The duration of the OVS sequence is clearly dominated by the BIR-4 tipdown pulse, which could be replaced by a shorter adiabatic pulse for faster OVS and less T_2^+ decay at the expense of B_1^+ robustness and saturation bandwidth. Alternatively, to improve tolerance to B_1^+ field variation, a longer BIR-4 pulse or a tailored saturation (15) sequence could be substituted. In these cases, the tipdown pulse parameters need to be chosen to maximize coherency and a new lookup table generated for OVS calibration.

The proposed design is compatible with other magnetization preparation techniques. For preparation sequences applied before OVS, there will be no adverse interferences as long as all transverse magnetization is dephased before OVS begins. It is therefore compatible with sequences such as adiabatic T_2 Prep (23) and spatial and spectral presaturations. It is also compatible with inversion preparations because inverted magnetization will assume the OVS spatial profile. Combining OVS with techniques such as double inversion black-blood preparation (24) will be effective for blood flowing through the cylindrical beam of the passband. For preparation sequences applied after OVS, shorter preparations are recommended because the stopband suppression will abate according to T_1.

The OVS sequence may be valuable in other imaging protocols. Scan times can be reduced in navigated acquisitions with OVS. Navigators positioned outside the passband beam may be attenuated, but in a cardiac protocol (25) the R-R interval will provide time for the navigator signal to regenerate. In flow-sensitive spiral acquisitions (26), the OVS sequence may improve spatial resolution and velocity estimation accuracy. The 2D multislice imaging protocol can be extended to a 3D acquisition of the cylindrical passband volume. Because one logical gradient is unused during the tipback pulse, profile variations along the cylinder may arise from spatially variant system imperfections. For real-time imaging, the OVS sequence could be applied at a frequency dictated by the local T_1 relaxation times. The high RF power of the BIR-4 pulse has minimal effects when applied once per R-R interval, as in this study. However, in other applications these effects may need further consideration when choosing the OVS repetition interval.

CONCLUSIONS

We have presented a new design for 2D OVS and rFOV imaging at 3 T. The proposed design has a short duration yet is still robust to B_1^+ attenuation. We have developed a solution to the Bloch equations using a small-tip angle approximation for transverse initial conditions, and formulated the solution to describe a general relationship between the spatial profiles of tipback pulses and conventional tipdown pulses. This relationship explains a unique property of spiral tipback pulses: single-shot pulses have the equivalent performance of two-shot pulses. The duration of the OVS sequence was kept to a minimum by exploiting this property. There was some loss of efficiency with the sequence, but for the cardiovascular imaging scenarios we considered this was acceptable. We have demonstrated the advantages of rFOV imaging, including reduced image artifacts and the ability to both prescribe and achieve finer spatial resolutions. The flexibility of the design permits a tradeoff between duration and SNR performance, and may be suitable for real-time imaging.

APPENDIX

Analysis of Small-Tip Pulses with Transverse Initial Magnetization

Here we formulate a general relationship between the magnetization spatial profiles of tipdown and tipback pulses with small flip angles. A similar analysis can be performed for frequency-selective and other types of small-tip pulses. We use the superscripts d and b to refer to the tipdown and tipback scenarios, respectively. Complex transverse magnetizations and RF waveforms are denoted as $M_{xy} = M_x + jM_y$ and $B_1 = B_{1,x} + jB_{1,y}$. When relaxation is ignored, the Bloch equations in the rotating frame are

$$\dot{M}_{xy} = -j\gamma(\boldsymbol{r}\cdot\boldsymbol{G})M_{xy} + j\gamma M_z B_1 \qquad [A1]$$

and

$$\dot{M}_z = \gamma B_{1,y}M_x - \gamma B_{1,x}M_y = -\gamma \mathrm{Im}\{B_1^* M_{xy}\}, \qquad [A2]$$

where * denotes complex conjugation.

In a conventional tipdown or excitation scenario, a pulse of duration T with RF waveform $B_1(t)$ and gradient waveform $\boldsymbol{G}(t)$ is applied to a spin system with longitudinal initial magnetization M_o. The spatial profile of the final transverse magnetization $M_{xy}^d(\boldsymbol{r})$ is formulated by solving the Bloch equations assuming a small flip angle so that $M_z^d \approx M_o$. The resulting spatial profile is

$$M_{xy}^d(\mathbf{r}) = j\gamma M_o \int_0^T B_1(\tau) e^{j\mathbf{r}\cdot\mathbf{k}^{\mathbf{d}}(\tau)} d\tau, \qquad [A3]$$

where $\boldsymbol{k}^{\boldsymbol{d}}(t) = -\gamma\int_t^T \boldsymbol{G}(s)ds$ is the conventional excitation k-space coordinate (11).

In the tipback scenario, the initial magnetization is transverse and the spatial profile of the final longitudinal magnetization $M_z^b(\boldsymbol{r})$ is desired. Define the initial magnetization to be $M_o e^{j\theta_o}$ with θ_o increasing counter-clockwise from $\hat{x}$. In a manner similar to the conventional small-tip approximation, we assume the tipback pulse rotates the magnetization vector out of the transverse plane by only a small amount so that $|M_{xy}^b| \approx M_o \gg M_z^b$. Equation A1

then decouples from Eq. A2, and the solution to Eq. A1 at time T becomes

$$M_{xy}^{b}(\mathbf{r}) \approx M_{o} e^{j\theta_{o}} e^{j\mathbf{r}\cdot\mathbf{k}_{c}}, \qquad [A4]$$

where $\boldsymbol{k_c} = -\gamma\int_0^T \boldsymbol{G}(s)ds$. The desired spatial profile of the tipback pulse is found by solving the system in Eqs. A2 and A4, which yields

$$M_{z}^{b}(\mathbf{r}) = -\gamma M_{o}\mathrm{Im}\left\{ e^{j\theta_{o}} \int_0^T B_1^*(\tau) e^{j\mathbf{r}\cdot\mathbf{k}^{\mathbf{b}}(\tau)} d\tau \right\}, \qquad [A5]$$

where $\boldsymbol{k^b}(t) = -\gamma\int_0^t \boldsymbol{G}(s)ds$. Note that $\boldsymbol{k_c} = \boldsymbol{k}^b(t) + \boldsymbol{k}^d(t)$.

If the tipback pulse has waveforms $B_1(t)$ and $\boldsymbol{G}(t)$ identical to the tipdown pulse, then the spatial profiles $M_z^b(\boldsymbol{r})$ and $M_{xy}^d(\boldsymbol{r})$ can be related. Substituting Eq. A3 in A5 yields

$$M_{z}^{b}(\mathbf{r}) = -\cos(\theta_{o} + \mathbf{r}\cdot\mathbf{k}_{\mathbf{c}}) M_{x}^{d}(\mathbf{r}) - \sin(\theta_{o} + \mathbf{r}\cdot\mathbf{k}_{\mathbf{c}}) M_{y}^{d}(\mathbf{r}). \qquad [A6]$$

The undesired spatial modulation can be removed by instead using waveforms $-B_1(T - t)$ and $\boldsymbol{G}(T - t)$ for the tipback pulse. Ignoring effects from relaxation and off resonance, these waveforms correspond to a direct reversal of the tipdown rotation process. With these waveforms, the spatial profile becomes

$$M_{z}^{b}(\mathbf{r}) = \cos(\theta_{o}) M_{x}^{d}(-\mathbf{r}) + \sin(\theta_{o}) M_{y}^{d}(-\mathbf{r}). \qquad [A7]$$

The space-reversal can be removed by using waveforms $-B_1^+(T - t)$ and $\boldsymbol{G}(T - t)$, which yields

$$M_{z}^{b}(\mathbf{r}) = -\cos\theta_{o} M_{x}^{d}(\mathbf{r}) + \sin\theta_{o} M_{y}^{d}(\mathbf{r}). \qquad [A8]$$

The modulation and space-reversal could also be removed from Eq. A6 by redesigning the pulse so that $\boldsymbol{k_c} = \mathbf{0}$.

This defines the general relationship between the tipdown and tipback scenarios for any small-tip pulse. When the initial magnetization is transverse, the final longitudinal magnetization is a weighted sum of the components of the final transverse magnetization had the initial magnetization been longitudinal. Fig. 3 illustrates this relationship for spiral pulses.

REFERENCES

1. Oppenheim AV, Schafer RW, Buck JR. Discrete-time signal processing. Upper Saddle River, NJ: Prentice-Hall; 1999.
2. Stenger AV, Boada FE, Noll DC. Multishot 3D slice-select tailored RF pulses for MRI. Magn Reson Med 2002;48:157–168.
3. Deng W, Stenger VA. A three-dimensional variable-density spiral spatial-spectral RF pulse with rotated gradients. Magn Reson Med 2010;63:828–834.
4. Haase A. Localization of unaffected spins in NMR imaging and spectroscopy (LOCUS spectroscopy). Magn Reson Med 1986;3:963–969.
5. Schaeffter T, Rasche V, Börnert P, Mens G. Interactive reduced FOV imaging for projection reconstruction and spiral acquisition. Magn Reson Imag 2001;19:677–684.
6. Le Roux PH, Gilles RJ, McKinnon GC, Carlier PG. Optimized outer volume suppression for single-shot fast spin-echo cardiac imaging. J Magn Reson Imag 1998;8:1022–1032.
7. Luo Y, de Graaf RA, DelaBarre L, Tannús A, Garwood M. BISTRO: an outer volume suppression method that tolerates RF field inhomogeneity. Magn Reson Med 2001;45:1095–1102.
8. Wilm BJ, Scensson J, Henning A, Pruessmann KP, Boesiger P, Kollias SS. Reduced field-of-view MRI using outer volume suppression for spinal cord diffusion imaging. Magn Reson Med 2007;57:625–630.
9. Schulte RF, Tsao J, Boesiger P, Pruessmann KP. Equi-ripple design of quadratic-phase RF pulses. J Magn Reson 2004;166:111–122.
10. Pisani L, Bammer R, Glover G. Restricted field of view magnetic resonance imaging of a dynamic time series. Magn Reson Med 2007;57:297–307.
11. Pauly J, Nishimura D, Macovski A. A k-space analysis of small-tip-angle excitation. J Magn Reson 1989;81:43–56.
12. Tannús A, Garwood M. Adiabatic pulses. NMR Biomed 1997;10:423–434.
13. Garwood M, Ke Y. Symmetric pulses to induce arbitrary flip angles with compensation for RF inhomogeneity and resonance offsets. J Magn Reson 1991;94:511–525.
14. Staewen RS, Johnson AJ, Ross BD, Parrish T, Merkle H, Garwood M. 3-D FLASH imaging using a single surface coil and a new adiabatic pulse, BIR-4. Invest Radiol 1990;25:559–567.
15. Sung K, Nayak KS. Design and use of tailored hard pulse trains for uniformed saturation of myocardium at 3 Tesla. Magn Reson Med 2008;60:997–1002.
16. Schär M, Vonken EJ, Stuber M. Simultaneous B0- and B_1^+-map acquisition for fast localized shim, frequency, and RF power determination in the heart at 3T. Magn Reson Med 2010;63:419–426.
17. Meyer CH, Pauly JM, Macovski A, Nishimura DG. Simultaneous spatial and spectral selective excitation. Magn Reson Med 1990;15:287–304.
18. Hoge RD, Kwan RK, Pike GB. Density compensation functions for spiral MRI. Magn Reson Med 1997;38:117–128.
19. Noll DC, Meyer CH, Pauly JM, Nishimura DG, Macovski A. A homogeneity correction method for magnetic resonance imaging with time-varying gradients. IEEE Trans Med Imaging 1991;10:629–637.
20. Duyn JH, Yang Y, Frank JA, van der Veen JW. Simple correction method for k-space trajectory deviations in MRI. J Magn Reson 1998;132:150–153.
21. Stanisz GJ, Odrobina EE, Pun J, Escaravage M, Grahan SJ, Bronskill MJ, Henkelman RM. T1 and T2 relaxation and magnetization transfer in tissue at 3T. Magn Reson Med 2005;54:507–512.
22. Noeske R, Seifert F, Rhein KH, Rinneberg H. Human cardiac imaging at 3T using phased array coils. Magn Reson Med 2000;44:978–982.
23. Nezafat R, Stubar M, Ouwerkerk R, Gharib AM, Desai MY, Pettigrew RI. B1-insensitive T2 preparation for improved coronary magnetic resonance angiography at 3 T. Magn Reson Med 2006;55:858–864.
24. Edelman RR, Chien D, Kim D. Fast selective black blood MR imaging. Radiology 1991;181:655–660.
25. Botnar RM, Stuber M, Kissinger KV, Kim WY, Spuentrup E, Manning WJ. Noninvasive coronary vessel wall and plaque imaging with magnetic resonance imaging. Circ 2000;102:2582–2587.
26. Brandts A, Stijntje RD, Doornbos J, Weiss RG, de Roos A, Stuber M, Westenberg JJM. Right coronary artery flow velocity and volume assessment with spiral k-space sampled breathhold velocity-encoded MRI at 3 Tesla: accuracy and repdoducibility. J Magn Reson Imaging 2010;31:1215–1223.